Chiral Metamaterials with *PT* Symmetry and Beyond

Sotiris Droulias[1,2*], Ioannis Katsantonis[1,2], Maria Kafesaki[1,2], Costas M. Soukoulis[1,3] and Eleftherios N. Economou[1,4]**

[1]*Institute of Electronic Structure and Laser, Foundation for Research and Technology Hellas, 71110 Heraklion, Crete, Greece*
[2]*Department of Materials Science and Technology, University of Crete, 71003 Heraklion, Greece*
[3]*Ames Laboratory and Department of Physics and Astronomy, Iowa State University, Ames, Iowa 50011, USA*
[4]*Department of Physics, University of Crete, 71003 Heraklion, Greece*
*e-mail: sdroulias@iesl.forth.gr
**e-mail: kafesaki@iesl.forth.gr

Supplementary Material

1. Conditions for *PT*-symmetry in chiral metamaterials

To find the conditions for *PT*-symmetry in systems with chiral response we first cast Maxwell's equations $\nabla \times \mathbf{E} = i\omega\mathbf{B}$, $\nabla \times \mathbf{H} = -i\omega\mathbf{D}$ into an eigenproblem of the form $\overline{\overline{\mathsf{H}}}\mathbf{F} = \omega\mathbf{F}$, where $\overline{\overline{\mathsf{H}}}$ is a pseudo-Hamiltonian tensor operator and $\mathbf{F}$ a generalized vector containing the fields. The constitutive relations are expressed according to Condon's convention [38] as $\mathbf{D} = \varepsilon\varepsilon_0\mathbf{E} + i(\kappa/c)\mathbf{H}$ and $\mathbf{B} = \mu\mu_0\mathbf{H} - i(\kappa/c)\mathbf{E}$, where ε, μ refer to the relative permittivity and permeability, respectively, κ is the chirality parameter and c the vacuum speed of light. If $\mathbf{F}$ is expressed in terms of $\mathbf{E}$ and $\mathbf{H}$, the magneto-electric coupling in the constitutive relations does not allow for the problem to be cast as in the non-chiral case in [22], because the eigenvalue ω appears in the generalized Hamiltonian $\overline{\overline{\mathsf{H}}}$ as well. Instead, if $\mathbf{F}$ is expressed in terms of $\mathbf{B}$, $\mathbf{D}$, a proper formulation is possible:

$$\overline{\overline{\mathsf{H}}}\begin{bmatrix} \mathbf{B} \\ \mathbf{D} \end{bmatrix} = \omega\begin{bmatrix} \mathbf{B} \\ \mathbf{D} \end{bmatrix} \tag{S1}$$

with $\overline{\overline{\mathsf{H}}}$ denoting a tensor operator that admits a Cartesian representation in terms of a 6×6 matrix:

$$\overline{\overline{\mathsf{H}}} = \begin{bmatrix} -i\overline{\overline{\Phi}}_{11}(\mathbf{r}) - i\phi_{11}(\mathbf{r})\overline{\overline{\Omega}}(\mathbf{r}) & -i\overline{\overline{\Phi}}_{12}(\mathbf{r}) - i\phi_{12}(\mathbf{r})\overline{\overline{\Omega}}(\mathbf{r}) \\ +i\overline{\overline{\Phi}}_{21}(\mathbf{r}) + i\phi_{21}(\mathbf{r})\overline{\overline{\Omega}}(\mathbf{r}) & +i\overline{\overline{\Phi}}_{22}(\mathbf{r}) + i\phi_{22}(\mathbf{r})\overline{\overline{\Omega}}(\mathbf{r}) \end{bmatrix} \tag{S2}$$

The tensors $\overline{\overline{\Omega}}(\mathbf{r})$, $\overline{\overline{\Phi}}_{ij}(\mathbf{r})$ represent Cartesian implementations of the 3-D curl operator:

$$\overline{\overline{\Omega}}(\mathbf{r}) = \begin{bmatrix} 0 & -\dfrac{\partial}{\partial z} & \dfrac{\partial}{\partial y} \\ \dfrac{\partial}{\partial z} & 0 & -\dfrac{\partial}{\partial x} \\ -\dfrac{\partial}{\partial y} & \dfrac{\partial}{\partial x} & 0 \end{bmatrix} \quad \text{(S3a)} \quad \text{and} \quad \overline{\overline{\Phi}}_{ij}(\mathbf{r}) = \begin{bmatrix} 0 & -\dfrac{\partial\phi_{ij}(\mathbf{r})}{\partial z} & \dfrac{\partial\phi_{ij}(\mathbf{r})}{\partial y} \\ \dfrac{\partial\phi_{ij}(\mathbf{r})}{\partial z} & 0 & -\dfrac{\partial\phi_{ij}(\mathbf{r})}{\partial x} \\ -\dfrac{\partial\phi_{ij}(\mathbf{r})}{\partial y} & \dfrac{\partial\phi_{ij}(\mathbf{r})}{\partial x} & 0 \end{bmatrix}, i,j = \{1,2\} \tag{S3b}$$

The scalar quantities $\phi_{ij}(\mathbf{r})$, which appear in $\overline{\overline{\Phi}}_{ij}(\mathbf{r})$ and $\overline{\overline{\mathsf{H}}}$ explicitly, are functions of the material parameters, and read as

$$\phi_{11}(\mathbf{r}) = -\frac{i\kappa/c}{\left(\varepsilon\mu - \kappa^2\right)/c^2}, \phi_{12}(\mathbf{r}) = +\frac{\mu\mu_0}{\left(\varepsilon\mu - \kappa^2\right)/c^2}, \phi_{21}(\mathbf{r}) = +\frac{\varepsilon\varepsilon_0}{\left(\varepsilon\mu - \kappa^2\right)/c^2}, \phi_{22}(\mathbf{r}) = +\frac{i\kappa/c}{\left(\varepsilon\mu - \kappa^2\right)/c^2} \tag{S4}$$

(for simplicity we have omitted the $\mathbf{r}$-dependence in ε, μ and κ). One can be convinced by performing the matrix multiplication shown in Eq. (S1) and taking into account Eqs (S2) to (S4) that this is a way of just rewriting Maxwell's equations.

For the eigenvalues of $\overline{\overline{H}}$ to be real, we require that $\overline{\overline{H}}$ is *PT*-symmetric [21,22], that is $\overline{\overline{H}}(\mathbf{r},t)=\overline{\overline{H}}^{*}(-\mathbf{r},-t)$ (S5)

Noting that $PT\left(i\overline{\overline{\Omega}}(\mathbf{r})\right)=i\overline{\overline{\Omega}}(\mathbf{r})$ and $PT\left(i\overline{\overline{\Phi}}_{ij}(\mathbf{r})\right)=PT\left(i\overline{\overline{\Omega}}(\mathbf{r})\overline{\overline{\mathrm{diag}}}\left(\phi_{ij}(\mathbf{r})\right)\right)=i\overline{\overline{\Omega}}(\mathbf{r})\overline{\overline{\mathrm{diag}}}\left(\phi_{ij}^{*}(-\mathbf{r})\right)$, condition (S5) yields:

$$\phi_{ij}(\mathbf{r})=\phi_{ij}^{*}(-\mathbf{r}),\ i,j=\{1,2\} \tag{S6}$$

where $\overline{\overline{\mathrm{diag}}}\left(\phi_{ij}(\mathbf{r})\right)$ is a diagonal 3×3 matrix consisting of the scalar quantities $\phi_{ij}(\mathbf{r})$, as given by Eq. (S4).

This condition is necessary but not sufficient; for a *PT*-symmetric Hamiltonian with nondegenerate spectrum to have real eigenvalues, the eigenvectors $\mathbf{F}$ should be also *PT*-symmetric [21], i.e. $PT\mathbf{F}=\mathbf{F}$. The eigenvectors of $\overline{\overline{H}}$ appear as pairs of RCP/LCP waves, $\mathbf{F}_{+}$, $\mathbf{F}_{-}$, which are not *PT*-symmetric under the space reversal $\mathbf{r}\rightarrow-\mathbf{r}$. However, because they share a common (degenerate) eigenvalue ω ($\overline{\overline{H}}\mathbf{F}_{+}=\omega\mathbf{F}_{+}$ $\underline{\mathrm{and}}$ $\overline{\overline{H}}\mathbf{F}_{-}=\omega\mathbf{F}_{-}$), this eigenvalue can be real if certain symmetries are preserved; for example, if the action of the *PT*-operator transforms the eigenvectors between RCP and LCP, i.e. if $PT\mathbf{F}_{+}=\mathbf{F}_{-}$ and $PT\mathbf{F}_{-}=\mathbf{F}_{+}$, then, for *PT*-symmetric $\overline{\overline{H}}$ (i.e. $PT\overline{\overline{H}}=\overline{\overline{H}}PT$), we can act on both sides of $\overline{\overline{H}}\mathbf{F}_{+}=\omega\mathbf{F}_{+}$ with the *PT* operator and transform this relation as $\overline{\overline{H}}\mathbf{F}_{+}=\omega\mathbf{F}_{+}\Rightarrow PT\overline{\overline{H}}\mathbf{F}_{+}=PT\omega\mathbf{F}_{+}\Rightarrow\overline{\overline{H}}PT\mathbf{F}_{+}=\omega^{*}PT\mathbf{F}_{+}\Rightarrow\overline{\overline{H}}\mathbf{F}_{-}=\omega^{*}\mathbf{F}_{-}$. The relation $PT\omega\mathbf{F}_{+}=\omega^{*}PT\mathbf{F}_{+}$ follows because the time reversal operator has the form of a matrix times the complex conjugation operator. Taking into account that $\overline{\overline{H}}\mathbf{F}_{-}=\omega\mathbf{F}_{-}$, we conclude that $\omega^{*}=\omega$, i.e. ω is real. Real eigenvalues can be achieved, for example, in systems with a reduced space reversal $x\rightarrow x$, $y\rightarrow y$, $z\rightarrow-z$, for waves propagating along the *z*-direction, as we have considered in the main manuscript. In such systems, the condition for $\overline{\overline{H}}$ to be *PT*-symmetric is simplified as $\phi_{ij}(z)=\phi_{ij}^{*}(-z)$ and inspection of Eq. (S4) yields the result presented in the main paper:

$$\varepsilon(z)=\varepsilon^{*}(-z),\ \mu(z)=\mu^{*}(-z)\ \text{and}\ \kappa(z)=-\kappa^{*}(-z) \tag{S7}$$

2. Analytical results for the double slab model

To find the reflection and transmission amplitudes of the double-slab system (which is surrounded by air), we assume that waves arrive at normal incidence from either side of the system and we solve Maxwell's equations, applying the boundary conditions at each material interface. The waves propagate along the *z*-direction as shown in Fig. S1 and their polarization vector, which lies on the *xy*-plane, can be either linear or circular. To satisfy the *PT*-symmetry requirements (S7), we are interested in material parameters of certain spatial symmetry; however, we start with slabs of arbitrary properties, ε_i, μ_i, κ_i and L_i, to obtain general expressions (the subscript $i=\{g,l\}$ denotes the '*gain*' and '*loss*' regions respectively). Due to the two possible circular polarizations at each of the two sides – Right/Left Circularly Polarized (RCP/LCP or +/–) waves, the system can be described by four input and four output ports and hence by a 4×4 scattering matrix, consisting of eight reflection and eight transmission coefficients, $\{r, t\}$. Due to chirality there are two wavenumbers $k_i^{\pm}=k_0\left(\sqrt{\varepsilon_i\mu_i}\pm\kappa_i\right)$ in each region, the one (+) corresponding to RCP waves and the other (–) corresponding to LCP waves (k_0 is the free space wavenumber).
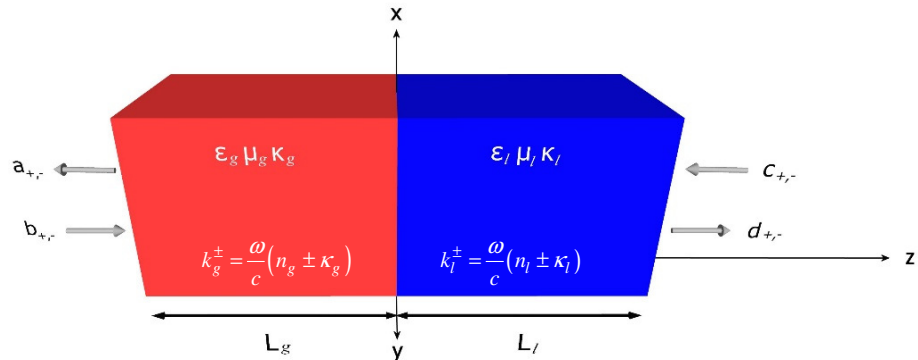

Figure S1: Schematic of the double slab model. The complex material parameters ε_i, μ_i and κ_i are the relative permittivity, the relative permeability and the chirality parameter, respectively, and the subscript $i=\{g,l\}$ denotes whether they are located in the '*gain*' or the '*loss*' region. The parameters $n_i=(\varepsilon_i\mu_i)^{1/2}$ and k_i are the corresponding refractive index and wavenumber. The amplitudes of the incident (b,c) and scattered (a,d) waves are shown, where the subscript +/– accounts for Right/Left Circularly Polarized (RCP/LCP or +/–) waves. Due to chirality there are two wavenumbers in each region, k_i^{+}/k_i^{-} corresponding to RCP (+) / LCP (–) waves, respectively.

The analytical results for Linearly Polarized and Circularly Polarized incident waves are listed below. The letter *L/R* in the subscript denotes incidence from 'Left' or 'Right' and the remaining two symbols denote the output and incident polarization.

2.1 Scattering coefficients for Linearly Polarized (LP) waves:

LP wave incident from LEFT (subscript *L*):   **LP wave incident from RIGHT (subscript *R*):**

$$t_{L,xx} = -4e^{-ik_0(L_g+L_l)}\left(e^{i(L_g k_g^+ + L_l k_l^+)} + e^{i(L_g k_g^- + L_l k_l^-)}\right)\frac{1}{A+B}$$

$$t_{R,xx} = t_{L,xx}$$

$$t_{L,yx} = -4ie^{-ik_0(L_g+L_l)}\left(e^{i(L_g k_g^+ + L_l k_l^+)} - e^{i(L_g k_g^- + L_l k_l^-)}\right)\frac{1}{A+B}$$

$$t_{R,yx} = -t_{L,yx}$$

$$r_{L,xx} = -e^{-2iL_g k_0}\frac{C_L + D_L}{A+B}$$

$$r_{R,xx} = -e^{-2iL_l k_0}\frac{C_R + D_R}{A+B} \qquad (\text{S8})$$

$$r_{L,yx} = 0$$

$$r_{R,yx} = 0$$

$$t_{L,yy} = t_{L,xx},\ t_{L,xy} = -t_{L,yx},\ r_{L,yy} = r_{L,xx},\ r_{L,xy} = r_{L,yx} \qquad\qquad t_{R,yy} = t_{R,xx},\ t_{R,xy} = -t_{R,yx},\ r_{R,yy} = r_{R,xx},\ r_{R,xy} = r_{R,yx}$$

2.2 Scattering coefficients for Circularly Polarized (CP) waves:

CP wave incident from LEFT (subscript *L*):   **CP wave incident from RIGHT (subscript *R*):**

$$t_{L,++} = -8e^{i(L_g k_g^+ + L_l k_l^+ - (L_g+L_l)k_0)}\frac{1}{A+B}$$

$$t_{R,++} = t_{L,++}\left(\stackrel{\triangle}{=} t_{++}\right)$$

$$t_{L,--} = -8e^{i(L_g k_g^- + L_l k_l^- - (L_g+L_l)k_0)}\frac{1}{A+B}$$

$$t_{R,--} = t_{L,--}\left(\stackrel{\triangle}{=} t_{--}\right)$$

$$r_{L,+-} = -e^{-2iL_g k_0}\frac{C_L + D_L}{A+B}$$

$$r_{R,+-} = -e^{-2iL_l k_0}\frac{C_R + D_R}{A+B} \qquad (\text{S9})$$

$$r_{L,-+} = r_{L,+-}\left(\stackrel{\triangle}{=} r_L\right)$$

$$r_{R,-+} = r_{R,+-}\left(\stackrel{\triangle}{=} r_R\right)$$

$$t_{L,+-} = t_{L,-+} = r_{L,++} = r_{L,--} = 0 \qquad\qquad t_{R,+-} = t_{R,-+} = r_{R,++} = r_{R,--} = 0$$

where:

$$A = Z_g\left(+\left(\frac{1}{Z_g}+1\right)+\left(\frac{1}{Z_g}-1\right)e^{iL_g(k_g^+ + k_g^-)}\right)\left(-\left(\frac{1}{Z_l}+1\right)+\left(\frac{1}{Z_l}-1\right)e^{iL_l(k_l^+ + k_l^-)}\right) \qquad (\text{S10})$$

$$B = Z_l\left(-\left(\frac{1}{Z_g}+1\right)+\left(\frac{1}{Z_g}-1\right)e^{iL_g(k_g^+ + k_g^-)}\right)\left(+\left(\frac{1}{Z_l}+1\right)+\left(\frac{1}{Z_l}-1\right)e^{iL_l(k_l^+ + k_l^-)}\right)$$

$$C_L = Z_g\left(+\left(\frac{1}{Z_g}+1\right)e^{iL_g(k_g^+ + k_g^-)}+\left(\frac{1}{Z_g}-1\right)\right)\left(+\left(\frac{1}{Z_l}-1\right)e^{iL_l(k_l^+ + k_l^-)}-\left(\frac{1}{Z_l}+1\right)\right)$$

$$D_L = Z_l\left(+\left(\frac{1}{Z_g}+1\right)e^{iL_g(k_g^+ + k_g^-)}-\left(\frac{1}{Z_g}-1\right)\right)\left(+\left(\frac{1}{Z_l}-1\right)e^{iL_l(k_l^+ + k_l^-)}+\left(\frac{1}{Z_l}+1\right)\right)$$

$$C_R = Z_g\left(+\left(\frac{1}{Z_g}-1\right)e^{iL_g(k_g^+ + k_g^-)}+\left(\frac{1}{Z_g}+1\right)\right)\left(+\left(\frac{1}{Z_l}+1\right)e^{iL_l(k_l^+ + k_l^-)}-\left(\frac{1}{Z_l}-1\right)\right)$$

$$D_R = Z_l\left(+\left(\frac{1}{Z_g}-1\right)e^{iL_g(k_g^+ + k_g^-)}-\left(\frac{1}{Z_g}+1\right)\right)\left(+\left(\frac{1}{Z_l}+1\right)e^{iL_l(k_l^+ + k_l^-)}+\left(\frac{1}{Z_l}-1\right)\right)$$

The parameter $Z_i = \sqrt{\mu_i/\varepsilon_i}$, $i = \{g,l\}$, is the wave impedance, which is normalized to the free-space impedance $Z_0 = \sqrt{\mu_0/\varepsilon_0}$.

The terms A, B, C_L, C_R, D_L, D_R consist of the wave impedances Z_g, Z_l (both independent of chirality) and terms of the form $e^{iL_g(k_g^+ + k_g^-)} = e^{ik_0 L_g (n_g + \kappa_g + n_g - \kappa_g)} = e^{2ik_0 L_g n_g}$ and $e^{iL_l(k_l^+ + k_l^-)} = e^{ik_0 L_l (n_l + \kappa_l + n_l - \kappa_l)} = e^{2ik_0 L_l n_l}$. These terms do not contain κ_g or κ_l and hence *the reflection coefficients are independent of chirality*. On the other hand, the transmission coefficients consist of terms of the form $e^{i(L_g k_g^\pm + L_l k_l^\pm)} = e^{ik_0(L_g n_g \pm L_g \kappa_g + L_l n_l \pm L_l \kappa_l)} = e^{ik_0(L_g n_g + L_l n_l)} e^{\pm ik_0(L_g \kappa_g + L_l \kappa_l)}$. Hence, although generally chirality-dependent, the *transmission can be tuned independently from chirality if $L_g\kappa_g + L_l\kappa_l = 0$*. In particular, Re($\kappa$) is responsible for phase changes in t, while Im(κ) for amplitude changes (note that, while the sign of Im(n) accounts for gain or loss, the sign of Im(κ) expresses the difference in absorption between RCP/LCP waves, i.e. it does not imply gain). These conclusions are also evident in the calculated optical activity θ and ellipticity η [34]:

Optical activity:
$$\theta = \frac{1}{2}\left(\arg(t_{++}) - \arg(t_{--})\right) \Rightarrow \quad \theta = \frac{1}{2} 2k_0 \left(L_g \operatorname{Re}(\kappa_g) + L_l \operatorname{Re}(\kappa_l)\right) \tag{S11}$$

Ellipticity:
$$\eta = \frac{1}{2}\sin^{-1}\left(\frac{|t_{++}|^2 - |t_{--}|^2}{|t_{++}|^2 + |t_{--}|^2}\right) \Rightarrow \quad \eta = \frac{1}{2}\sin^{-1}\left(\frac{1 - \exp\left[4k_0\left(L_g \operatorname{Im}(\kappa_g) + L_l \operatorname{Im}(\kappa_l)\right)\right]}{1 + \exp\left[4k_0\left(L_g \operatorname{Im}(\kappa_g) + L_l \operatorname{Im}(\kappa_l)\right)\right]}\right) \tag{S12}$$

To summarize, the effect of chirality appears in transmission as $L_g\kappa_g + L_l\kappa_l \neq 0$, with κ_g, κ_l complex in general, and does not affect the reflection, which behaves as if the system was non-chiral. A nonzero Re($L_g\kappa_g + L_l\kappa_l$) results to $|t_{++}| = |t_{--}|$, but causes phase changes in t_{++}, t_{--} and hence nonzero optical activity θ. A nonzero Im($L_g\kappa_g + L_l\kappa_l$) causes $|t_{++}| \neq |t_{--}|$ and hence nonzero ellipticity η. In particular, for slabs of the same thickness $L_g = L_l = L/2$ (as in *PT*-symmetric systems) we find:

$$\theta = \frac{1}{2}k_0 L\left(\operatorname{Re}(\kappa_g) + \operatorname{Re}(\kappa_l)\right) \text{ and } \eta = \frac{1}{2}\sin^{-1}\left(\frac{1 - \exp\left[2k_0 L\left(\operatorname{Im}(\kappa_g) + \operatorname{Im}(\kappa_l)\right)\right]}{1 + \exp\left[2k_0 L\left(\operatorname{Im}(\kappa_g) + \operatorname{Im}(\kappa_l)\right)\right]}\right)$$

These formulas verify the results presented in the main manuscript. For example, for fully *PT*-symmetric systems where $\kappa_g = -\kappa_l^*$ (as in Fig.2a, Fig.4a), $\operatorname{Re}(\kappa_g) = -\operatorname{Re}(\kappa_l) \Rightarrow \theta = 0$; if $\kappa_g = \kappa_l^*$ (as in Fig.2b, Fig.4b), then $\operatorname{Im}(\kappa_g) = -\operatorname{Im}(\kappa_l) \Rightarrow \eta = 0$.

Last, if $\kappa_g = -\kappa_l$, i.e. $\begin{cases} \operatorname{Re}(\kappa_g) = -\operatorname{Re}(\kappa_l) \\ \operatorname{Im}(\kappa_g) = -\operatorname{Im}(\kappa_l) \end{cases} \Rightarrow \begin{cases} \theta = 0 \\ \eta = 0 \end{cases}$. This case is referred in the main manuscript as 'spatially balanced chirality' and corresponds to the case where the system responds macroscopically as non-chiral, despite having local chirality,

3. Alternative representations of the scattering matrix

As already mentioned, due to the two possible circular polarizations at each of the two sides of the double slab model, the system can be described by four input and four output ports and hence by a 4×4 scattering matrix S, consisting of eight reflection and eight transmission coefficients, $\{r, t\}$. Depending on the arrangement of the $\{r, t\}$ elements on the 4×4 matrix, i.e. on the arrangement of the input and output ports, the S-matrix can be formulated in several ways. Hence, depending on each choice, the S-matrix may have different eigenvalues, which reveal different aspects of the scattering process. In our case, the main information we are concerned with is related to the PT properties of our system. In other words, we would like to know which one is the appropriate S-matrix formulation that will give us information about the position of the Exceptional Point.

Although different S-matrix formulations may yield different eigenvalues, they all share a common property; because they are rearrangements of the same set of matrix elements, they all have the same poles in the complex frequency plane. Hence, the system has a unique description in terms of its poles. The poles of a PT system have a very distinctive behavior; below the Exceptional Point they are all located in the lower imaginary plane and split into two branches above the Exceptional Point regardless of the S-matrix formulation [18]. Our analytical model allows us to perform analytic continuation in the complex plane and examine the poles of the S-matrix. In turn, this directly indicates the appropriate S-matrix formulation, the eigenvalues of which show the distinct regions of PT and broken PT-phase. Such a procedure was also followed in [18] in order to resolve the same issue in the non-chiral case. Here, our analytical model serves likewise as a means for identifying the appropriate representation, which can be then used in real experiments. Below we list some selected formulations and their corresponding eigenvalues:

type 1:

$$\begin{pmatrix} a_+ \\ a_- \\ d_+ \\ d_- \end{pmatrix} = \begin{pmatrix} r_{L,++} & r_{L,+-} & t_{R,++} & t_{R,+-} \\ r_{L,-+} & r_{L,--} & t_{R,-+} & t_{R,--} \\ t_{L,++} & t_{L,+-} & r_{R,++} & r_{R,+-} \\ t_{L,-+} & t_{L,--} & r_{R,-+} & r_{R,--} \end{pmatrix} \begin{pmatrix} b_+ \\ b_- \\ c_+ \\ c_- \end{pmatrix} = \overbrace{\begin{pmatrix} 0 & r_L & t_{++} & 0 \\ r_L & 0 & 0 & t_{--} \\ t_{++} & 0 & 0 & r_R \\ 0 & t_{--} & r_R & 0 \end{pmatrix}}^{S_1} \begin{pmatrix} b_+ \\ b_- \\ c_+ \\ c_- \end{pmatrix}$$

with four eigenvalues $s_{1,2,3,4} = \pm\dfrac{1}{\sqrt{2}}\sqrt{r_L^2 + r_R^2 + t_{++}^2 + t_{--}^2 \pm \sqrt{\left((r_L + r_R)^2 + (t_{++} - t_{--})^2\right)\left((r_L - r_R)^2 + (t_{++} + t_{--})^2\right)}}$

type 2:

$$\begin{pmatrix} a_+ \\ a_- \\ d_+ \\ d_- \end{pmatrix} = \begin{pmatrix} r_{L,++} & r_{L,+-} & t_{R,+-} & t_{R,++} \\ r_{L,-+} & r_{L,--} & t_{R,--} & t_{R,-+} \\ t_{L,++} & t_{L,+-} & r_{R,+-} & r_{R,++} \\ t_{L,-+} & t_{L,--} & r_{R,--} & r_{R,-+} \end{pmatrix} \begin{pmatrix} b_+ \\ b_- \\ c_- \\ c_+ \end{pmatrix} = \overbrace{\begin{pmatrix} 0 & r_L & 0 & t_{++} \\ r_L & 0 & t_{--} & 0 \\ t_{++} & 0 & r_R & 0 \\ 0 & t_{--} & 0 & r_R \end{pmatrix}}^{S_2} \begin{pmatrix} b_+ \\ b_- \\ c_- \\ c_+ \end{pmatrix}$$

with four eigenvalues $s_{1,2} = \dfrac{1}{2}\left(+r_L + r_R \pm \sqrt{(r_L - r_R)^2 + 4t_{++}t_{--}}\right)$, $s_{3,4} = \dfrac{1}{2}\left(-r_L + r_R \pm \sqrt{(r_L + r_R)^2 - 4t_{++}t_{--}}\right)$

type 3:

$$\begin{pmatrix} a_- \\ d_+ \\ a_+ \\ d_- \end{pmatrix} = \begin{pmatrix} r_{L,-+} & t_{R,--} & r_{L,--} & t_{R,-+} \\ t_{L,++} & r_{R,+-} & t_{L,+-} & r_{R,++} \\ r_{L,++} & t_{R,+-} & r_{L,+-} & t_{R,++} \\ t_{L,-+} & r_{R,--} & t_{L,--} & r_{R,-+} \end{pmatrix} \begin{pmatrix} b_+ \\ c_- \\ b_- \\ c_+ \end{pmatrix} = \overbrace{\begin{pmatrix} r_L & t_{--} & 0 & 0 \\ t_{++} & r_R & 0 & 0 \\ 0 & 0 & r_L & t_{++} \\ 0 & 0 & t_{--} & r_R \end{pmatrix}}^{S_3} \begin{pmatrix} b_+ \\ c_- \\ b_- \\ c_+ \end{pmatrix}$$

with two eigenvalues $s_{1,2} = \dfrac{1}{2}\left(+r_L + r_R \pm \sqrt{(r_L - r_R)^2 + 4t_{++}t_{--}}\right)$

As mentioned earlier, the denominators in r, t do not depend on chirality and hence the S-matrix poles are expected to be identical to those of the non-chiral counterpart. Indeed, our simulations agree with this theoretical conclusion and therefore the last S-matrix formulation, S_3, provides the most suitable eigenvalue set and is the one that we have used throughout this paper. The poles of all scattering matrices S_1, S_2 and S_3 together with their eigenvalues are shown in Fig. S2 for the example shown in Fig. 2 in the main manuscript (also reproduced here in the bottom panels of Fig S2, for comparison).
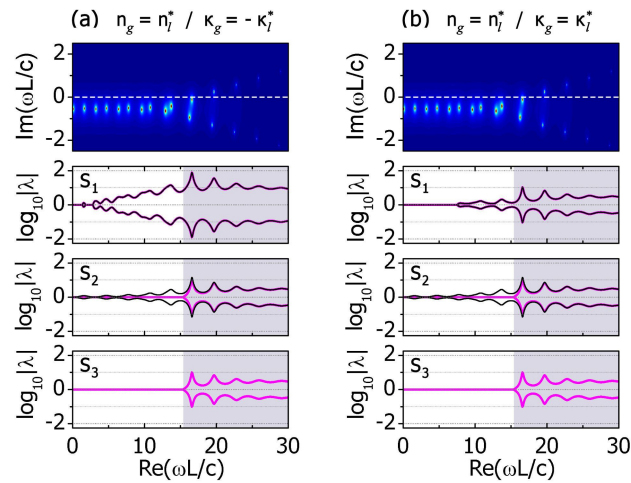

Figure S2: Poles and eigenvalues of the scattering matrix S. Here, the *PT* chiral system of Fig. 2 of the main manuscript is examined. The system has length L, $n = 2\pm0.2i$ and chirality (a) $\kappa = \pm0.165+0.165i$ and (b) $\kappa = 0.165\pm0.165i$. The top row depicts the poles of the S-matrix and the eigenvalues of the S_1, S_2 and S_3 representations are shown below. The eigenvalues of S_1 change with chirality and those of S_2 identify the Exceptional Point only partly. The eigenvalues of S_3 do not depend on chirality and are therefore the most suitable eigenvalue set.

4. Generalized unitarity relation and experimental identification of Exceptional Point

The analytical expressions for the generalized unitarity relation and the experimental criterion for locating the Exceptional Point correspond to the results introduced in [18], with the simple substitution $T \to \sqrt{T_{++}T_{--}}$, where $T_{++} \equiv |t_{++}|^2$ and $T_{--} \equiv |t_{--}|^2$. In particular:

The experimental criterion for locating the Exceptional Point was found in [18] to follow from the break of unitarity of the S-matrix eigenvalues. In our case, due to $t_{++}t_{--} = t_{nonchiral}^2$, the eigenvalues of S_3 are identical to those of its non-chiral counterpart and hence the conclusions for $t_{nonchiral}$ in [18] hold here for $\sqrt{t_{++}t_{--}}$, i.e. the substitution $t_{nonchiral} \to \sqrt{t_{++}t_{--}}$ yields the respective conclusions for our chiral system. Hence, using the result of Eq. (17) in [18] and substituting $T \to \sqrt{T_{++}T_{--}}$ we obtain:

$$\frac{R_L + R_R}{2} - \sqrt{T_{++}T_{--}} = 1$$

where $R_L \equiv |r_L|^2$ and $R_R \equiv |r_R|^2$.

The generalized unitarity relation was shown in [18] to follow from the fact that $\text{Det}M = 1$, where M is the transfer matrix, and the condition $M^{-1} = M^*(\omega^*)$ which is a direct consequence of the imposed *PT*-symmetry conditions [15]. In our case, the transfer matrix M_3 that corresponds to S_3 can be easily shown to satisfy $\text{Det}M_3 = 1$ as well. Using this result in combination with the demand for $M_3^{-1} = M_3^*(\omega^*)$, after some calculations we find:

$$\left| \sqrt{T_{++}T_{--}} - 1 \right| = \sqrt{R_L R_R}$$

This result is equivalent to the result of Eq. (9) in [18] with the substitution $T \to \sqrt{T_{++}T_{--}}$.

5. Configuration of realistic Chiral Metamaterial (CMM) and numerical calculations of scattering parameters

The basic Chiral Metamaterial (CMM) block that has been used in our simulations consists of two metallic crosses twisted with respect to each other and embedded in a dielectric host of low index, $n_{host} = 1.41$. The two metallic crosses are made of gold, the permittivity of which is modeled by a Drude response: $\varepsilon(\omega) = \varepsilon_\infty - \omega_p^2/(\omega^2+i\omega\gamma)$, with $\varepsilon_\infty = 9.07$, $\omega_p = 2\pi\times2159$ THz and $\gamma = 2\pi\times25$ THz. To achieve the *PT*-CMM we introduce an imaginary part in n_{host} to model gain and we also tune the twist between the two crosses as an additional control on the achieved effective chirality. The unit cell of the CMM is periodically repeated on the *xy*-plane, forming an infinite metamaterial sheet of thickness *w*. All geometrical parameters are shown in Fig. S3.
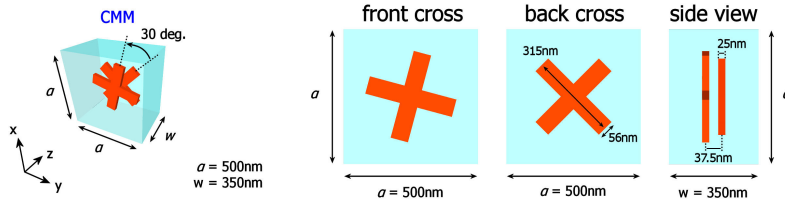

Figure S3: Unit cell of the CMM used in our simulations. Two metallic crosses are twisted with respect to each other and embedded in a dielectric host of low index, $n_{host} = 1.41$. The twist between the two crosses is used for external control on the achieved effective chirality.

In the simulations we first excite the system with a circularly polarized wave from the left side and for each incident polarization (RCP/LCP or +/−) we measure the reflected and transmitted waves in the two polarizations as well, ending up with eight measurements. Then we repeat the same procedure for excitation from the right side and we calculate the 2×8 = 16 scattering parameters r_{ij}, t_{ij} where $i,j = \{+, -\}$. After we arrange all r_{ij}, t_{ij} in the scattering matrix S_3 we calculate its eigenvalues, which we plot in Fig. 4 and in this document. We also plot the scattered power $R_{ij} = |r_{ij}|^2$, $T_{ij} = |t_{ij}|^2$ and use t_{++}, t_{--} to calculate the optical rotation θ and ellipticity η.

6. Expected results for system under perfect *PT*-conditions and further examples

Because there is a slight discrepancy between conditions (1) and the retrieved parameters for our CMM and *PT*-CMM (see Fig. 3 of the main manuscript), we have already pointed out that some deviation from the perfect *PT*-symmetric system is to be expected. In order to demonstrate that *this deviation is quantitative only* and to predict the behavior of the system under perfect *PT*-conditions, we use the numerically retrieved parameters ε_{CMM}, μ_{CMM} and κ_{CMM} and we artificially set $\varepsilon_{PT-CMM} = (\varepsilon_{CMM})^*$, $\mu_{PT-CMM} = (\mu_{CMM})^*$ and $\kappa_{PT-CMM} = -(\kappa_{CMM})^*$. Then we replace the actual CMM/*PT*-CMM structures with homogeneous slabs of the same effective parameters and solve the equivalent model of four homogeneous slabs analytically. In Fig. S4 we present these theoretical calculations and, for comparison, we repeat the numerical results presented in Fig.3,4a in the main manuscript. The tuning parameter ε'' is scanned within the broader range [-2.5, 2.5], where the sign change means that the positions of the auxiliary gain/slab pair are interchanged. Because the effective parameters at the two outer slabs are not interchanged, we observe two asymmetric Exceptional Points, located at $\varepsilon'' = -1.74$ and $\varepsilon'' = +0.88$ (the shaded regions denote the broken *PT*-phase). The results verify conditions (2) and demonstrate the existence of ATRs close to $\varepsilon'' = \pm 1$. The theoretical results are shown in Fig. S4b (left panel) and the full-wave simulations of the actual configuration are shown in Fig. S4b (right panel). The agreement is excellent, despite the slight discrepancy between the retrieved parameters and the strict *PT* conditions (1). This can be visualized in the eigenvalues λ of the scattering matrix (top row) and the generalized unitarity relation (5) (dashed line in middle row), which are slightly modified in comparison to the ideal system. As for the chiral parameters, we have already mentioned that the *PT*-conditions impose $\theta = 0$, but due to the non-perfect match of the chiral parameters there is a residual optical rotation θ. However, the positions of the Exceptional Point and the ATRs are in excellent agreement with the ideally expected. In order to examine the results of Fig. 4b in a similar manner we artificially set $\varepsilon_{PT-CMM} = (\varepsilon_{CMM})^*$, $\mu_{PT-CMM} = (\mu_{CMM})^*$ and $\kappa_{PT-CMM} = (\kappa_{CMM})^*$ and we solve the analytical model of four homogeneous slabs, which is shown in Fig. S4d (left panel). For comparison, in Fig. S4d (right panel) we repeat the numerical results of the actual configuration. Again the agreement is excellent and these calculations verify that the Exceptional Point is not affected by changes in chirality and hence, the *PT*-symmetry aspect is independent of the chiral aspect, as predicted by our simple model.
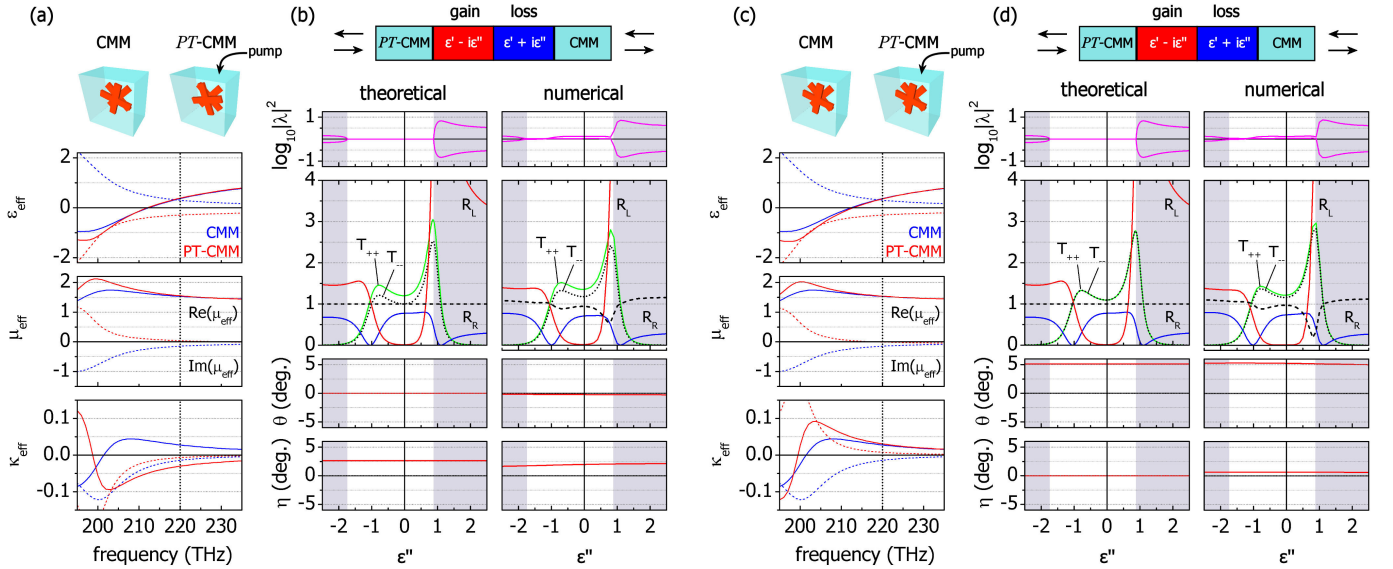

Figure S4: Comparison between perfect *PT*-conditions ('theoretical') and realistically achieved ('numerical') with the chosen metamaterial for (a),(b) $\kappa_{PT-CMM} = -(\kappa_{CMM})^*$ and (c),(d) $\kappa_{PT-CMM} = (\kappa_{CMM})^*$. (a), (c) Retrieved parameters. (b), (d) Analytical (left panel) and numerical (right panel) calculations. The results in (a),(c) and right panels of (b),(d) correspond to the results presented in Fig. 3 and 4.

In order to demonstrate the basic principles of our analysis, the examples of the realistic structures presented in the main paper were chosen so as to satisfy conditions (1) primarily for ε and μ. This choice provided us with relatively weak chiral effects as compared to the advanced capabilities of chiral metamaterials. To demonstrate that our choice does not imply a limitation on the chiral effects, here we use the same system to satisfy *PT* conditions at different frequencies, where the chirality is stronger. Because in this work we are not interested in optimized configurations, the deviation from conditions (1) at the chosen frequencies is allowed to be slightly larger. However, Exceptional Points and ATRs are still present and are now accompanied by strong chiral effects. In Fig. S5 we demonstrate three such cases. We use the CMM and *PT*-CMM of the main manuscript and move to a new operation frequency, which is marked with a vertical dotted line in Fig. S5b (for each case individually). To control the chiral effects we tune the twist between the crosses. The notation for the twist is shown in Fig. S5a and a positive

$\theta_{CMM}/\theta_{PT\text{-}CMM}$ corresponds to a clockwise mutual twist, where the twist direction refers to the cross located closest to the side of the observer. The results for each corresponding case are shown in Fig. S5c. Starting with the exact configuration of Fig. S4a,b (θ_{CMM} = -30deg. / $\theta_{PT\text{-}CMM}$ +30deg.) but changing the operation frequency to 166THz where the effective chirality is stronger, we achieve θ = 16deg. and η = -14deg. (left panels in Fig. S5b,c). If we twist the crosses only of *PT*-CMM in the opposite direction (θ_{CMM} = -30deg. / $\theta_{PT\text{-}CMM}$ -30deg.) we achieve θ = -19deg. and η = 0 (middle panels in Fig. S5b,c) at a slightly higher frequency. There we achieve enhanced Re(κ), while cancelling Im(κ). Finally, in the latter configuration, by twisting the crosses of both CMM and *PT*-CMM in the opposite direction (θ_{CMM} = +30deg. / $\theta_{PT\text{-}CMM}$ +30deg.) we reverse the sign of optical rotation, thus achieving θ = +19deg. and η = 0 (right panels in Fig. S5b,c). In this case we manage to reverse the sign of the effective chirality κ and, thus reversing the sign of Re(κ), while maintaining the cancellation of Im(κ). For the two latter cases, in particular, (Fig. S5b,c, middle and right panel) the simulations verify that the sign of optical rotation can be tuned without affecting the Exceptional Point and the ATRs. These results support our finding that the chirality can be tailored independently of permittivity and permeability, thus enabling versatile control of the system's properties.
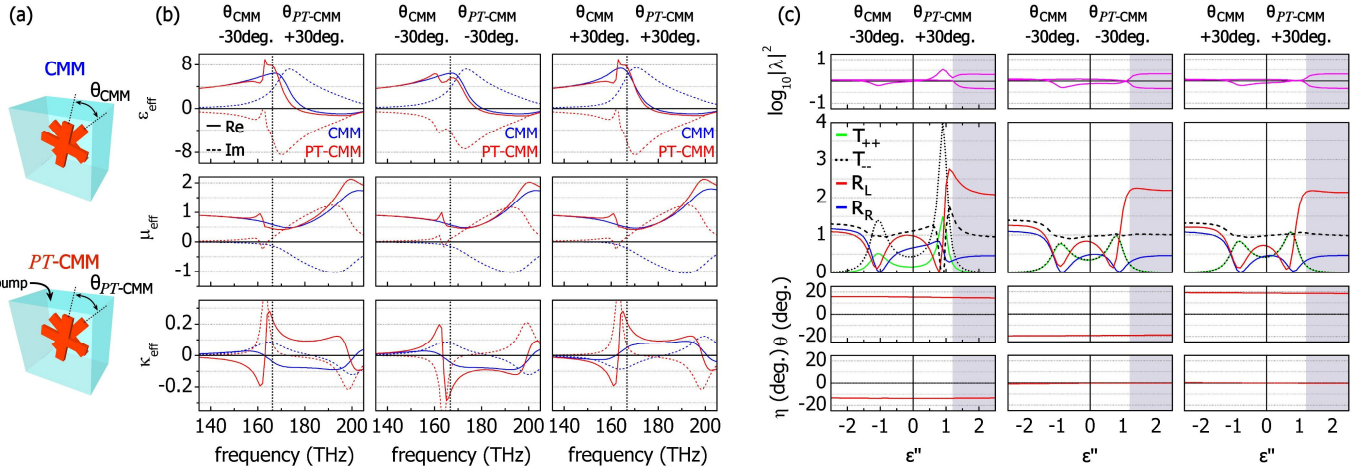

Figure S5: Examples of strong chiral response and demonstration of external control. We use the CMM and *PT*-CMM of the main manuscript and change only the twist between the crosses as depicted in (a) and the operation frequency, which is marked as a vertical dotted line in (b), for each individual case. (b) Retrieved parameters and (c) numerical calculations for the three cases shown on top of each panel.

7. Tuning the ATRs

The presented realistic examples were chosen for demonstration and do not necessarily imply the need for large amounts of gain (ε''~1). As an example, below we present a (non-optimized) modified version of our system shown in Fig.4, in which we scan the length of the auxiliary gain/loss slab pair to show that it is possible to observe similar features with significantly less gain. The parameters are all the same as in Fig. 4 and the operation point presented in the main paper is marked here with the vertical dashed line (corresponding to slabs of 500nm length).
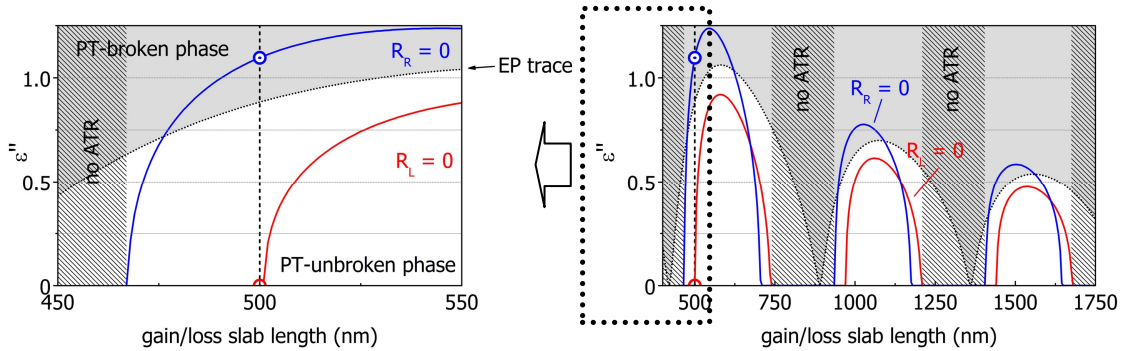

Figure S6: ATRs as function of the gain/loss (ε'') and length of the auxiliary slab pair. The blue (red) lines correspond to ATRs for the R_R (R_L) reflectance and the regions where no ATRs are possible are marked with the vertical shaded zones. The trace of the Exceptional Point is marked with the dotted line and the broken *PT*-phase is designated with the gray area. The left panel shows the 450nm-550nm range in detail, while the right panel extends the scan up to 1750nm to show that, with increasing slab length, even less gain is required.